INORGANIC CHEMISTRY FRONTIERS

RESEARCH ARTICLE

View Article Online
View Journal | View Issue

Cite this: *Inorg. Chem. Front.*, 2022, **9**, 6457

Wheel-shaped molybdenum(v) cobalt-phosphate cluster as a highly sensitive bifunctional photoelectrochemical sensor for the trace determination of Cr(vi) and tetracycline†

Xiu-Juan Zhang, Yuan-Yuan Ma, * Hao-Xue Bi, Xiao-Yu Yin, Hao Song, Man-Hui Liu and Zhan-Gang Han *

Developing highly sensitive detection technology for trace heavy metal and antibiotic pollutants in water systems is vital to ensure environmental safety and human health. Here, one wheel-shaped $\{Co_{16}Mo_{16}P_{24}\}$ cluster-based framework was hydrothermally synthesized with the formula $\{[Co(H_2O)_6][Co_{12}(BBTZ)_6][(Mo_2O_4)_8(HPO_4)_{22}(PO_4)_2Co_4(H_2O)_8]\}\cdot 45H_2O$ (**1**) (BBTZ = 1,4-bis(1,2,4-triazol-1-ylmethyl)benzene), which was employed as a bifunctional photoelectrochemical sensor for the determination of trace Cr(vi) and tetracycline (TC). In crystal **1**, wheel-shaped $\{Co_{16}Mo_{16}P_{24}\}$ clusters with a diameter of 19.4 Å act as six-connected nodes to coordinate with BBTZ ligands, extending into a robust three-dimensional framework with a *pcu* topology. Crystal **1** possesses wide light absorption and excellent redox properties, which displayed remarkable bifunctional photoelectrochemical response towards the Cr(vi) reduction and TC oxidation. The detection limit (LOD) of hybrid **1** for Cr(vi) is 24.62 nM and the sensitivity for Cr(vi) determination is 216.76 μA μM^{-1}. Similarly, hybrid **1** exhibits a high sensitivity of 315.94 μA μM^{-1} and a low LOD of 33.45 nM for TC detection. These parameters are far superior to the standards set by the WHO and the EU. Importantly, sensor **1** possesses high anti-interference ability and performs well in real lake water and milk samples. This work provides some guidance for the development of promising crystalline photoelectrochemical sensors for practical environmental monitoring.

Received 7th September 2022,
Accepted 14th October 2022

DOI: 10.1039/d2qi01936a

rsc.li/frontiers-inorganic

1. Introduction

Environmental pollution has become a serious problem that hinders the sustainable development of the economy and threatens human health. In particular, various non-biodegradable and highly toxic pollutants, such as heavy metal ions, antibiotics, pesticides, *etc.*, have been casually discharged into the water environment, which destroys the original water ecosystem and seriously endangers the health of organisms and humankind.[1] The highly toxic heavy metal contaminant hexavalent chromium (Cr(vi)) has been widely used in electroplating, and dye and leather manufacturing industries.[2] Since it can enter cells to damage DNA and other cell components, even Cr(vi) in trace amounts has been well known as a kind of carcinogen, and genotoxic and mutagen agent.[3] Tetracycline, as one representative of antibiotics, possesses economy and broad-spectrum antibacterial activity and has been widely used to treat infections in humans and animals caused by Gram-positive and Gram-negative bacteria.[4–6] However, the abuse application of TC generates the drug resistance of bacteria and results in high residue in lots of environmental areas and animal products.[7,8] The World Health Organization (WHO) has set the maximum total amount of Cr(vi) allowed in potable water to be 50 μg L^{-1} (0.05 ppm), and the European Union (EU) has set the standard that the maximum residue limits for TC cannot exceed 100 μg kg^{-1} in milk and muscle tissues.[9] Thus, it is of paramount significance to develop a sensitive, rapid and reliable technique to achieve accurate supervision of Cr(vi) and TC pollution in water samples.

Nowadays, various sensing methods, including fluorescence, electrochemical, chromatography, and photoelectrochemical techniques, *etc.* have been developed for the detection of water contaminants.[10–12] Among them, photoelectrochemical (PET) analysis has attracted widespread attention

Hebei Key laboratory of Organic Functional Molecules, National Demonstration Center for Experimental Chemistry Education, College of Chemistry and Materials Science, Hebei Normal University, Shijiazhuang, Hebei 050024, P. R. China. E-mail: mayy334@hebtu.edu.cn, hanzg116@126.com

†Electronic supplementary information (ESI) available: Chemicals, instruments, measurements, and X-ray crystallography, Fig. S1–S6, Tables S1–S5. CCDC 2178098. For ESI and crystallographic data in CIF or other electronic format see DOI: https://doi.org/10.1039/d2qi01936a

owing to its unique benefits encompassing high sensitivity, low background signal, simple operation, and easy miniaturization.[13,14] In a typical PEC sensor, the light source excites the photoactive sensor materials to accelerate the electron transfer process between the catalytic sites and the analyte, converting the light irradiation into a magnified electrical signal with a dose–response relationship with the analyte.[15] Thus PEC sensors are expected to achieve efficient determination of trace Cr(VI) and TC in water environments. For now, some PEC sensors are developed for monitoring Cr(VI) or TC individually.[16–19] However, the development of a low-cost, ultrasensitive, rapid response and multi-functional PEC sensor is still highly desired for the monitoring of Cr(VI) and TC.

As a unique class of multifunctional materials with versatile architectures, polyoxometalates (POMs) exhibit tremendous applications in photocatalysis,[20–22] electrocatalysis,[23–25] energy conversion and materials[26] owing to their unmatched physical and chemical properties. In the POM family, a wheel-shape molybdenum(V) cobalt-phosphate cluster with the general formula $[(Mo_2O_4)_8(PO_4)_{24}Co_{16}(H_2O)_{20}]^{10-}$ (denoted as $\{Co_{16}Mo_{16}P_{24}\}$) has drawn great attention because of its fully reduced oxidation state of the Mo element and high structural symmetry.[27–29] The wheel-shaped $\{Co_{16}Mo_{16}P_{24}\}$ cluster was constructed by the alternating connection of four groups of Mo^V–Co^{II} tetramers. The low oxidation state of the Mo element can not only increase the surface charge density and activate the surface oxygen atoms of the $\{Co_{16}Mo_{16}P_{24}\}$ cluster, but also endow it with specific redox properties, reversible multi-electron transfer properties and broad spectral absorption. For example, Su *et al.* demonstrated that a $\{Co_{16}Mo_{16}P_{24}\}$ cluster has a narrow band gap and a wide range of visible light absorption. Combined with $[Ru(bpy)_3]^{2+}$ species, the composite presents high photocatalytic activity for syngas production from diluted CO_2.[30] Our previous work found that the fully reduced phosphomolybdates show great potential in the electrochemical detection of Cr(VI) because of the fast and reversible electron transfer properties.[31,32] These advantages make the $\{Co_{16}Mo_{16}P_{24}\}$ cluster an ideal candidate for the construction of efficient photoelectrochemical sensors. Since Sécheresse *et al.* reported the first example of the $\{Co_{16}Mo_{16}P_{24}\}$ cluster in 2001,[27] the investigation into this area is relatively slow and only several structures consisting of isolated $\{Co_{16}Mo_{16}P_{24}\}$ clusters were reported. The high-dimensional frameworks constructed by $\{Co_{16}Mo_{16}P_{24}\}$ cluster are lacking and $\{Co_{16}Mo_{16}P_{24}\}$-based materials are much less studied as photoelectrochemical sensors. Therefore, it should be hopeful to exploit efficient functional photoelectrochemical sensors by employing $\{Co_{16}Mo_{16}P_{24}\}$-based materials for the determination of trace Cr(VI) and TC, which is of great concern for the environmental safety, but remains a great challenge.

Herein, one 3D hybrid based on a wheel-shaped $\{Co_{16}Mo_{16}P_{24}\}$ cluster, $\{[Co(H_2O)_6][Co_{12}(BBTZ)_6][(Mo_2O_4)_8(HPO_4)_{22}(PO_4)_2Co_4(H_2O)_8]\}\cdot 45H_2O$ (**1**) (BBTZ = 1,4-bis(1,2,4-triazol-1-ylmethyl) benzene), was successfully synthesized and used as a bifunctional photoelectrochemical sensor for trace determination of Cr(VI) and TC. In hybrid **1**, $\{Co_{16}Mo_{16}P_{24}\}$ clusters act as six-connected nodes to link each other *via* BBTZ ligands into a robust three-dimensional framework with a *pcu* topology. Benefiting from the intrinsic light-absorption capacity and excellent redox property, hybrid **1** displayed a remarkable dual-functional photoelectrochemical response towards Cr(VI) reduction and TC oxidation. The limit of detection (LOD) of hybrid **1** for Cr(VI) is 24.62 nM and the sensitivity for Cr(VI) determination is 216.76 μA μM^{-1}. As for TC, the LOD and sensitivity are 33.45 nM and 315.94 μA μM^{-1}, respectively. Such performance is far superior to the standards set by the WHO and the EU. Moreover, hybrid **1** possesses high anti-interference ability and performs well in the detection of Cr(VI) in natural water and TC in milk samples, providing a promising photoelectrochemical sensor for practical environmental monitoring.

2. Results and discussion

2.1 Structural analysis

Hybrid **1** was hydrothermally synthesized by reaction of sodium molybdate, phosphoric acid, cobalt chloride and BBTZ with a starting pH value of 2.0. Both a high mole ratio of Co : Mo and a high reaction temperature were necessary to achieve a $\{Co_{16}Mo_{16}P_{24}\}$ cluster. During the hydrothermal reaction, BBTZ ligands play the dual role of a reducing agent for reducing Mo^{VI} to Mo^V and a complexing agent to coordinate with Co centers, facilitating the formation of dark red crystals of hybrid **1** (Fig. S1†). Single crystal X-ray diffraction analysis showed that hybrid **1** crystallized in ther $P\bar{1}$ space group of the triclinic crystal system (Table S1†). The crystallographic asymmetric unit was composed of half a $\{Co_{16}Mo_{16}P_{24}\}$ cluster and three BBTZ ligands. The $\{Co_{16}Mo_{16}P_{24}\}$ cluster exhibited a typical centrosymmetric wheel-shaped structural feature with overall C_{4V} symmetry (Fig. 1). Such a wheel-shaped cluster with a diameter of 19.4 Å contains four $\{Mo_4\}$ tetramers, two $\{Co_4P_6N_4\}$ tetramers, and two $\{Co_4P_6N_2\}$ tetramers, with a

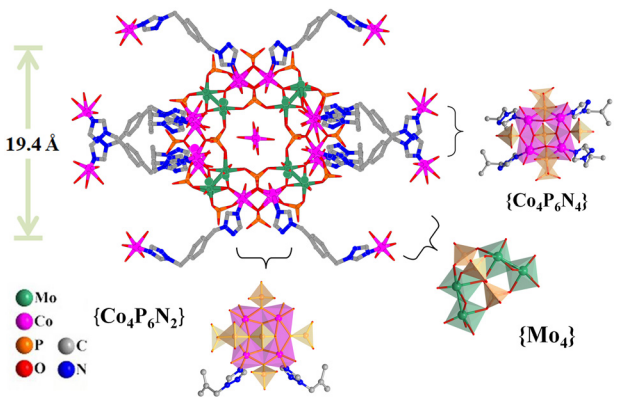

Fig. 1 Ball-stick representation of a wheel-shaped $\{Co_{16}Mo_{16}P_{24}\}$ cluster in hybrid **1**. Color code: Co, purple; Mo, green; O, red; N, blue; and P, orange.

central $[Co(H_2O)]_6^{2+}$ octahedron encapsulated in the inner space of the wheel (Fig. 1). The $\{Mo_4\}$ tetramer was constructed by four $\{MoO_6\}$ octahedra, which can be divided into two $\{Mo_2(\mu_2\text{-}O)_2\}$ dimers. The $\{Mo_2(\mu_2\text{-}O)_2\}$ dimer consists of two edge-sharing $\{MoO_6\}$ octahedra and further are linked together by three phosphate groups *via* one μ_3-oxygen and six μ_2-oxygen atoms. Notably, there are two Mo–Mo bonds in the $\{Mo_4\}$ tetramer with a distance of 2.60 Å, indicating the low valence states of Mo element in $\{Co_{16}Mo_{16}P_{24}\}$ (Tables S2 and S3†).

The tetramer of $\{Co_4P_6N_2\}$ consists of four distorted edge-shared octahedra, in which these Co^{II} centers are bridged through six phosphate groups, forming almost a square with angles of 89.47°–90.29°. In the $\{Co_4P_6N_2\}$ tetramer, two Co^{II} centers were six-coordinated with four μ_3-O donors from four phosphate groups, a terminal water molecule and one μ_2-O atom arising from the $\{Mo_2(\mu_2\text{-}O)_2\}$ group octahedron, while the other two Co^{II} centers coordinate with four μ_3-O atoms from four phosphate groups, one μ_2-O atom arising from the $\{Mo_2(\mu_2\text{-}O)_2\}$ group octahedron and one N donor from the BBTZ ligand. The $\{Co_4P_6N_4\}$ tetramer possesses a similar square structural feature to the $\{Co_4P_6N_2\}$ tetramer, in which each Co^{II} center is surrounded by four μ_3-O atoms from four phosphate groups, one μ_2-O atom arising from the $\{Mo_2(\mu_2\text{-}O)_2\}$ group octahedron and one N donor from the BBTZ ligand. The Co–O bond lengths in hybrid **1** are within the range of 1.98–2.30 Å, and the Co–N bond lengths range from 2.02 Å to 2.15 Å (Tables S2 and S3†). The three kinds of tetramers ($\{Mo_4\}$, $\{Co_4P_6N_4\}$ and $\{Co_4P_6N_2\}$) are alternatively connected with each other in a corner-sharing mode to form a wheel-shaped $\{Co_{16}Mo_{16}P_{24}\}$ cluster (Fig. 1). Therefore, compared to the reported parent $[(Mo_2O_4)_8(PO_4)_{24}Co_{16}(H_2O)_{20}]^{10-}$ cluster, twelve terminal water molecules of $\{Co_{16}Mo_{16}P_{24}\}$ in hybrid **1** are replaced by N donors of BBTZ ligands.

In hybrid **1**, BBTZ ligands display *cis*- and *trans*-configurations, which act as linkers to bridge the two Co^{II} centers from two adjacent $\{Co_{16}Mo_{16}P_{24}\}$ clusters (Fig. 2). Twelve Co^{II} centers in one $\{Co_{16}Mo_{16}P_{24}\}$ cluster coordinate with eight BBTZ ligands with a *trans*-configuration and four BBTZ ligands with a *cis*-configuration, respectively. These bridging ligands link the adjacent $\{Co_{16}Mo_{16}P_{24}\}$ clusters together into three-dimensional frameworks of hybrid **1** (Fig. 2a–c). Structurally, the wheel-shaped $\{Co_{16}Mo_{16}P_{24}\}$ cluster can be viewed as a six-connected node (each direction is a double connector), in which four *cis*-BBTZ ligands are attached to two $\{Co_{16}Mo_{16}P_{24}\}$ clusters in a perpendicular orientation, and eight *trans*-BBTZ ligands are linked to four $\{Co_{16}Mo_{16}P_{24}\}$ clusters in an equatorial orientation (Fig. 2c). Thus, the whole framework adopts a unimodal 6-connected *pcu* alpha-Po original cubic topology, in which the point symbol is $\{4^{12}\cdot6^3\}$ (Fig. 2e and f). Such a kind of framework endows hybrid **1** with high structural stability, and can facilitate substrate diffusion and mass transport during the photoelectrochemical detection process.

2.2 Physical characterization

To gain more insights into the composition and structure of hybrid **1**, a series of characterization studies namely FT-IR spectroscopy, X-ray photoelectron spectroscopy (XPS), X-ray diffraction (XRD) and TG analysis were conducted. Fig. S2a†

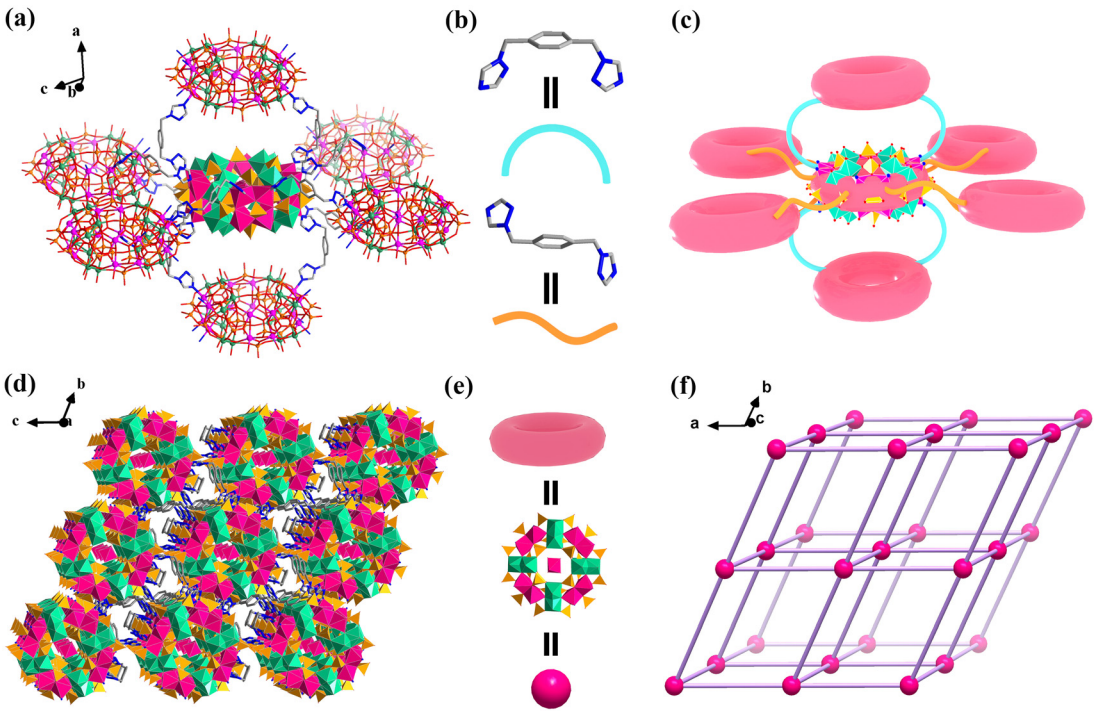

Fig. 2 (a) Ball and stick representations showing the connection mode of $\{Co_{16}Mo_{16}P_{24}\}$ clusters in **1** bridged by BBTZ ligands; (b) Schematic view of organic ligands in *cis* and *trans*-forms; (c) Schematic view of the connection mode of $\{Co_{16}Mo_{16}P_{24}\}$ clusters; (d) Ball-and-stick and polyhedral views of the 3D framework of **1**; (e) Sketch view of the wheel-shaped $\{Co_{16}Mo_{16}P_{24}\}$ cluster; (f) Schematic view of the *pcu* topology framework.

shows the IR spectrum of hybrid **1**. The characteristic absorption peaks at 683–1043 cm^{-1} were attributed to the stretching vibrations of the Mo–O–Mo, Mo═O and P–O bonds in the $\{Co_{16}Mo_{16}P_{24}\}$ cluster, and the strong characteristic peaks located in 1627 and 1666 cm^{-1} correspond to the ν (C═C) and ν (C═N) of the BBTZ ligand. The XRD patterns of the as-synthesized hybrid **1** display a good match with the result of theoretical simulations, which suggests high crystallinity and excellent phase purity of hybrid **1** (Fig. S2b†). The valence states of hybrid **1** were probed by the XPS spectrum and bond valence sum (BVS) calculation (Fig. S2c and Table S4†). As shown in Fig. S2c,† the Mo 3d XPS spectrum shows peaks at binding energies of 230.89 and 234.09 eV ascribed to Mo^{V} $3d_{5/2}$ and Mo^{V} $3d_{3/2}$,[33,34] which are in agreement with the BVS results. The low oxidation state of the Mo element in the $\{Co_{16}Mo_{16}P_{24}\}$ cluster can not only enhance the spectral absorption, but also endow it with reversible redox properties and fast electron transfer capacity. Moreover, TG analysis showed that hybrid **1** can maintain its structure up to 200 °C (Fig. S2d†), implying its high thermal stability. In general, the above results further demonstrated the structure of the wheel-shaped $\{Co_{16}Mo_{16}P_{24}\}$ cluster-based crystalline hybrid **1**.

2.3 Electro- and photo-chemical properties of hybrid 1

The electrochemical performance of hybrid **1** was examined in pH=0 H_2SO_4 electrolyte by the cyclic voltammetry (CV) technique. The CV curves in Fig. 3a shows three pairs of reversible peaks with mean peak potentials ($E_{1/2}$, $E_{1/2}$ = (E_{pa} + E_{pc})/2) of 189.5 mV (I–I′), 253 mV (II–II′) and 230 mV (III–III′), respectively. These reversible peaks are attributed to the multi-electron redox process of the Mo element in the $\{Co_{16}Mo_{16}P_{24}\}$ cluster (Table S5†), which reveals the excellent redox property of hybrid **1**. Since there is a linear correlation between the peak currents and the square root of the sweep velocity, the redox process on the surface of the catalyst is determined by the diffusion process. To assess the optical property of hybrid **1**, the UV-Vis diffuse reflection spectroscopy (DRS) and Mott–Schottoky measurements were carried out. As shown in Fig. 3b, hybrid **1** shows a broad and strong spectral absorption from 200 to 800 nm owing to its intrinsic semiconductor-like feature, signifying the potential of hybrid **1** as a photoelectrochemical sensor. The energy band gap (E_g) of 2.70 V was calculated using the Tauc plot derived from the equation $(\alpha h\nu)^2 = A(h\nu - E_g)^n$ (Fig. 3b). The Mott–Schottoky plot in Fig. 3c showed that the conduction band (CB) potential of hybrid **1** was calculated to be −0.53 V *vs.* Ag/AgCl, that is equivalent to −0.33 V *vs.* normal hydrogen electrode (NHE). Notably, the CB potential of hybrid **1** is more negative than the $E(O2/^{\bullet}O^{2-})$ of −0.33 eV and the CB position of Cr^{VI}/Cr^{III} (+0.51 V, pH = 6.8), suggesting that the photoreduction Cr(VI) on hybrid **1** is thermodynamically feasible. Moreover, the valence band (VB) potential of hybrid **1** is 2.37 eV *vs.* NHE. This value is more positive than the oxidation potential $E(H_2O/^{\bullet}OH)$ of +2.27 eV, disclosing the photooxidation TC capacity of hybrid **1**.[32,35] In addition, the transient photocurrent responses (*i*–*t* curves) of hybrid **1** showed large and stable photocurrent signals for four cycles of light on/off (Fig. 3d), showing its excellent photogenerated carrier separation efficiency. In general, the above results demonstrated the great potential of hybrid **1** as a photoelectrochemical catalyst for the photo-electrochemical determination of Cr(VI) and TC.

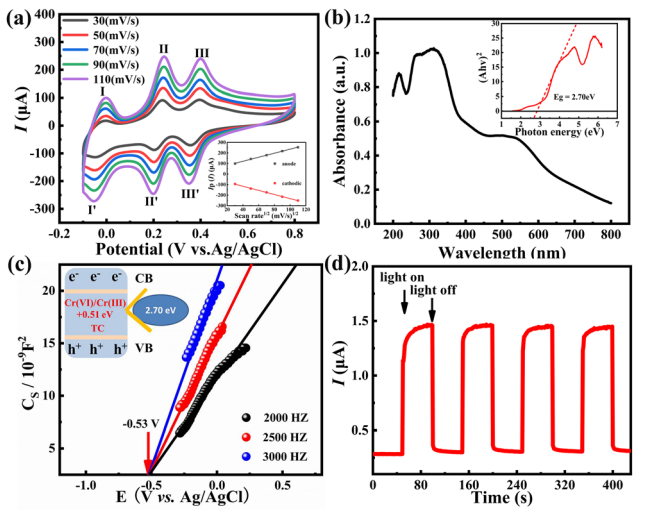

Fig. 3 (a) CV curves of hybrid **1** at different scan rates; (b) UV-vis diffuse reflection spectrum of **1**, inset: the corresponding plot of $(\alpha h\nu)^2$ *vs.* $h\nu$; (c) Mott–Schottky plots of **1** in 0.2 M Na_2SO_4 solution at pH = 6.80, insert: energy diagram of the HOMO and LUMO levels of **1**; (d) Transient photocurrent response of hybrid **1** within four cycles of light on/off.

2.4 Photoelectrochemical detection performance of hybrid 1 towards Cr(VI)

The photoelectrochemical detection activity of hybrid **1** was firstly explored in a 0.5 M H_2SO_4 electrolyte using trace Cr(VI) as a substrate. Before the test, a control experiment was done to evaluate the electrochemical properties of hybrid **1** towards Cr(VI) determination under dark conditions by applying the different pulse voltammetry (DPV) technique. As depicted in Fig. 4a, when the concentration of Cr(VI) in the electrolyte consecutively increases from 0.1 μM to 1.0 μM, sensor **1** exhibited steady increasing response currents, suggesting the fast and sensitive electrochemical responsiveness of hybrid **1** to the changes in Cr(VI) concentration. Fig. 4b shows a linear relationship between the Cr(VI) concentration and response current, which can be expressed by the linear regression formula I (μA) = −115.60 × C (μM) + 11.54, where C represents the Cr(VI) concentration and I represents the response current. On the basis of the S/N = 3 principle, the detection limit (LOD) of hybrid **1** for Cr(VI) is 46.17 nM (0.0048 ppm) and the sensitivity is 115.60 μA μM^{-1}, which far satisfies the WHO standard for Cr(VI) species in drinking water (≤ 0.05 ppm). Then, the photoelectrochemical performance of hybrid **1** towards Cr(VI) detection was investigated under the irradiation of white light with a power of 40 W (Fig. 4c and d). After the addition of 1.0 μM Cr(VI), the response current reached 207.59 μA, which was significantly larger than that under dark conditions (106.82 μA) (Fig. 4e), implying the remarkable photoelectrochemical

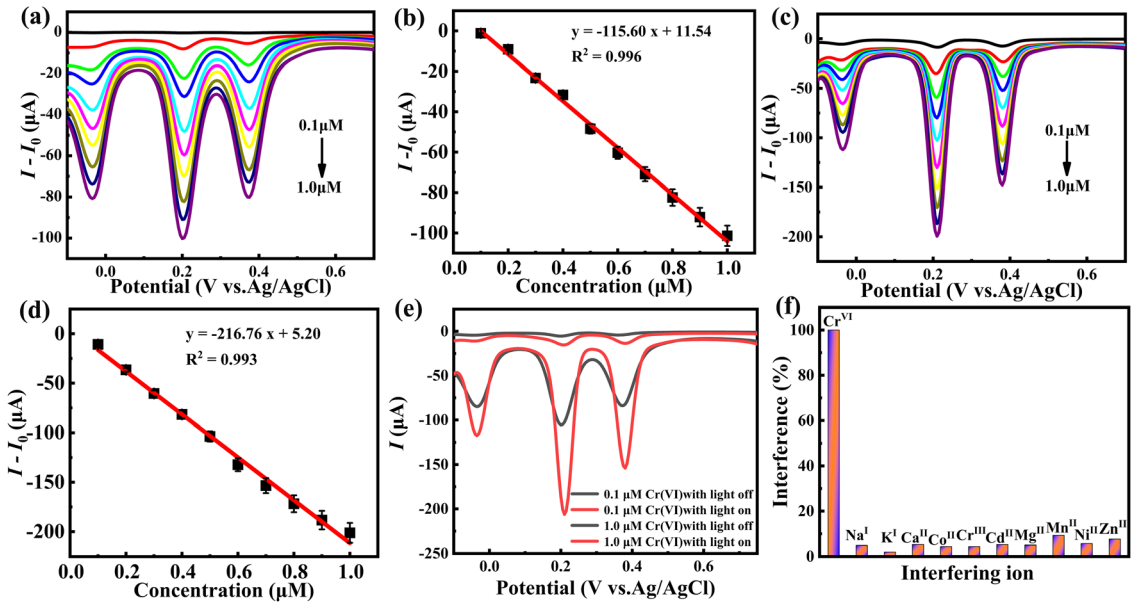

Fig. 4 (a) DPV curves of hybrid **1** modified electrodes in 0.5 M H_2SO_4 with continuous addition of Cr(VI) under dark conditions; (b) The corresponding linear dependences; (c) DPV curves of **1** in 0.5 M H_2SO_4 with successive changes in concentrations of 0.1 and 1.0 μM Cr(VI) under visible light illumination; (d) The linear dependence curve of **1**; (e) Control experiments showing DPV curves of **1** with continuous addition of Cr(VI) under dark or light illumination; (f) Current interference of **1** towards Cr(VI) with different interferents of 40 μM Na^+, K^+, Ca^{2+}, Co^{2+}, Cd^{2+}, Cr^{3+}, Mg^{2+}, Mn^{2+}, Ni^{2+}, and Zn^{2+} to mix with 4 μM Cr(VI), respectively.

activity towards Cr(VI) detection. Upon successive addition of Cr(VI) to the system, the DPV curves of hybrid **1** in Fig. 4d show an obvious linear relationship in the range of 0.1–1 μM with a linear regression equation of I (μA) = −216.76 × C (μM) + 5.20. In the light of this equation, the sensitivity of hybrid **1** for the photoelectrochemical detection of Cr(VI) is as high as 216.76 μA μM^{-1}, and the detection limit was calculated to be 24.62 nM. Compared with the results under dark conditions, the LOD of hybrid **1** for Cr(VI) was improved from 46.17 to 24.62 nM, and the sensitivity was enhanced from 115.60 to 216.76 μA μM^{-1}. These results manifest the prominent photoelectrochemical performance of hybrid **1** towards trace Cr(VI) detection. Such a high improvement in detection performance may be attributed to the efficient photogenerated carrier separation ability and reversible redox property along with the unique light absorption capacity of the $\{Co_{16}Mo_{16}P_{24}\}$ cluster in hybrid **1**. In order to obtain a further understanding of the electron transfer behaviour of hybrid **1** under light and dark conditions, electrochemical impedance spectroscopy (EIS) was measured. As shown in Fig. S3,† hybrid **1** displays a small charge transfer impedance value of 16.50 Ω upon light irradiation, which is lower than that under dark conditions (31.95 Ω). Considering that Cr(VI) detection is a reduction process, the electron in the electrocatalytic process is the active species to accelerate the reduction of the heavy metal ion Cr(VI) to achieve the purpose of rapid detection. Thus the above results disclose that the fast electron-transfer capacity and efficient photogenerated carrier separation ability of hybrid **1** can facilitate the electron transfer process during Cr(VI) reduction, amplifying the response towards Cr(VI) detection.

To explore the active species and activity origin of hybrid **1**, single inorganic $\{Co_{16}Mo_{16}P_{24}\}$ cluster and ligand BBTZ had been selected as a comparison. The inorganic $\{Co_{16}Mo_{16}P_{24}\}$ cluster was synthesized according to the reported literature. As shown in Fig. S4,† upon continuously adding Cr(VI) under dark conditions, the inorganic $\{Co_{16}Mo_{16}P_{24}\}$ cluster showed obvious current responses with a current increment of 80 μA. The linear regression equation is I (μA) = −79.03 × C (μM) + 3.10. The sensitivity and detection limit (LOD) were calculated to be 79.03 μA μM^{-1} and 117.77 nM (0.0122 ppm). Under light irradiation, the response current of the $\{Co_{16}Mo_{16}P_{24}\}$ cluster with the addition of 1 μM Cr(VI) was enhanced from 80 to 140 μA and the corresponding linear regression equation is I (μA) = −142.66 × C (μM) − 0.62, from which the sensitivity and LOD of the $\{Co_{16}Mo_{16}P_{24}\}$ cluster for Cr(VI) determination were calculated to be 142.66 μA μM^{-1} and 65.24 nM (0.0067 ppm), suggesting excellent photoelectrochemical detection performance for Cr(VI) ions. Moreover, the DPV curves of the BBTZ ligand were obtained to further rule out the effects of organic ligands on the detection performance. As shown in Fig. S5,† when BBTZ was used as a photoelectrochemical sensor, there is almost no current response towards the change in Cr(VI) concentration. These results suggested that the $\{Co_{16}Mo_{16}P_{24}\}$ cluster in hybrid **1** serves as the main active species. In comparison with the inorganic $\{Co_{16}Mo_{16}P_{24}\}$ cluster, hybrid **1** displayed higher sensitivities and lower LODs for the detection of Cr(VI), implying that the high detection performance of hybrid **1** should be attributed to the synergistic effect between the $\{Co_{16}Mo_{16}P_{24}\}$ cluster and the Co-ligand in a 3-D framework structure, which facilitates the electron transfer and accelerates the separation of photogenerated carriers.

Additionally, the electrochemical detection performance of hybrid **1** towards Cr(VI) is also superior to that of most reported electrocatalysts (Table 1).

To assess the selectivity of the PEC sensor hybrid **1** towards Cr(VI), the effects of other potentially interfering metal ions on the photoelectrochemical detection performance were examined. Fig. 4f shows the response of hybrid **1** towards Cr(VI) and other metal ions (Na^+, K^+, Ca^{2+}, Co^{2+}, Cr^{3+}, Cd^{2+}, Mg^{2+}, Mn^{2+}, Ni^{2+}, Zn^{2+}). It can be found that even when the concentration of the interfering metal ions is ten times higher than that of Cr(VI), there is only a slight current deviation of less than 10%, indicating that hybrid **1** as a PEC sensor has high selectivity for the determination of Cr(VI).

To further demonstrate the practicality of the PEC sensor, hybrid **1** was employed to detect Cr(VI) species in real water systems, such as lake water samples. As shown in Fig. 5, hybrid **1** displayed an apparent response current towards Cr(VI) in lake water samples with the linear regression formula I (μA) = −193.93 × C (μM) − 3.83, from which the limit of detection (LOD) of hybrid **1** for Cr(VI) determination is 27.52 nM and the sensitivity for Cr(VI) determination is 193.93 μA μM^{-1}. This result shows good agreement with the results obtained in a pure water system, implying that **1** has important practical significance. In addition, long-term stability is one of the most important indicators of PEC sensors. As shown in Fig. S6,† hybrid **1** can work continuously for more than 10 hours, and the corresponding response current remains basically unchanged, suggesting its high photoelectrochemical stability.

Table 1 Comparison of **1** with other reported sensors for the determination of Cr(VI)

Sensor materials	Method	Dark-LOD (μM)	Light-LOD (μM)	Ref.
1	DPV	0.046	0.024	This work
Fe_3O_4/MoS_2/GCE	*i–t*	0.5	—	36
Au NPs@carbon nanotubes	*i–t*	0.72	—	37
Au NPs@C SPE	DPV	0.85	—	38
1-CPE	*i–t*	4.3 × 103	—	39

GCE = glassy carbon electrode; SPE = screen printed electrode; 1-CPE = $[Ag_2^I(HL1)][Cr(OH)_6Mo_6O_{18}]\cdot H_2O$, L1 = 4-[2-(5-pyridin-4-yl-[1,2,4]triazol-1-yl)-ethyl]-morpholine.

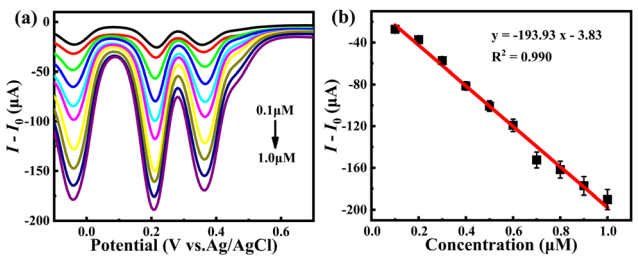

Fig. 5 (a) DPV curves of hybrid **1** in acidified lake water with successive additions of Cr(VI); (b) Its corresponding linear dependence plot.

2.5 Photoelectrochemical performance of hybrid 1 towards TC detection

As a bifunctional photoelectrochemical sensor, the photoelectrochemical activity of hybrid **1** for TC detection was also assessed by the DPV technique. First, the TC detection performance was investigated under dark conditions. As illustrated in Fig. 6a, the response current of hybrid **1** increased sharply when the TC concentration was continuously increased from 0.1 to 1.0 μM. With the addition of 1.0 μM TC, hybrid **1** produced a response current of 262.04 μA, which suggests the high sensitivity of hybrid **1** towards TC oxidation. Fig. 6b shows the linear relationship between the response peak current and TC concentrations in the range of 0.1–1.0 μM. The corresponding linear regression formula is I (μA) = 255.97 × C (μM) − 21.94, from which the LOD of hybrid **1** for TC determination is 41.28 nM and the sensitivity for TC determination is 255.97 μA μM^{-1}. When the TC analytic experiment was carried out under light illumination, a significant anodic current boost can be observed. As shown in Fig. 6c, with the addition of 0.1 μM and 1.0 μM TC, hybrid **1** produced response currents of 71.86 μA and 352.63 μA under light irradiation, which are 39.07 and 90.02 μA larger than that under dark conditions (32.79 and 262.61 μA), indicating the high photoelectrochemical activity of hybrid **1** toward TC detection. Furthermore, the DPV curves of hybrid **1** also displayed a distinct linear relationship between the response peak current and TC concentrations under light illumination with the linear regression formula I (μA) = 315.94 × C (μM) − 4.23 (Fig. 6d and e). The sensitivity of hybrid **1** as a PEC sensor for TC determination can reach 315.94 μA μM^{-1}, which is 1.23 times that under dark conditions. The LOD of the PEC sensor hybrid **1** for TC was calculated to be 33.45 nM, which is 7.83 nM lower than that under dark conditions. The photoelectrochemical performance of hybrid **1** toward TC detection far meets the standard set by the EU. For comparison, the $\{Co_{16}Mo_{16}P_{24}\}$ cluster produced a response current of 65 μA under dark with the addition of 1.0 μM TC and the corresponding sensitivity and LOD were 62.91 μA μM^{-1} and 66.92 nM. Under light irradiation, the response current with the addition of 1.0 μM TC was promoted to 125 μA. The sensitivity and LOD of the $\{Co_{16}Mo_{16}P_{24}\}$ cluster were enhanced to 128.62 μA μM^{-1} and 32.73 nM, respectively, further confirming the active species role of the $\{Co_{16}Mo_{16}P_{24}\}$ cluster (Fig. S7†). Similarly, BBTZ only showed a slight current response towards the concentration change of TC, further confirming that the active species in hybrid **1** is the $\{Co_{16}Mo_{16}P_{24}\}$ cluster (Fig. S8†).

In addition, the analytic selectivity and anti-interference of hybrid **1** were examined by adding selected interferents, glucose (Glu), levofloxacin (Lev) and sodium citrate (Sod Citr) into the TC detection system. Fig. 6f shows the percentage change in the current responses of hybrid **1** relative to 1 mM TC after the addition of 1 mM selected interferents. It can be seen that there is only a slight current disturbance in the detection of TC, indicating the favorable anti-interference and high selectivity of hybrid **1** towards TC oxidation.

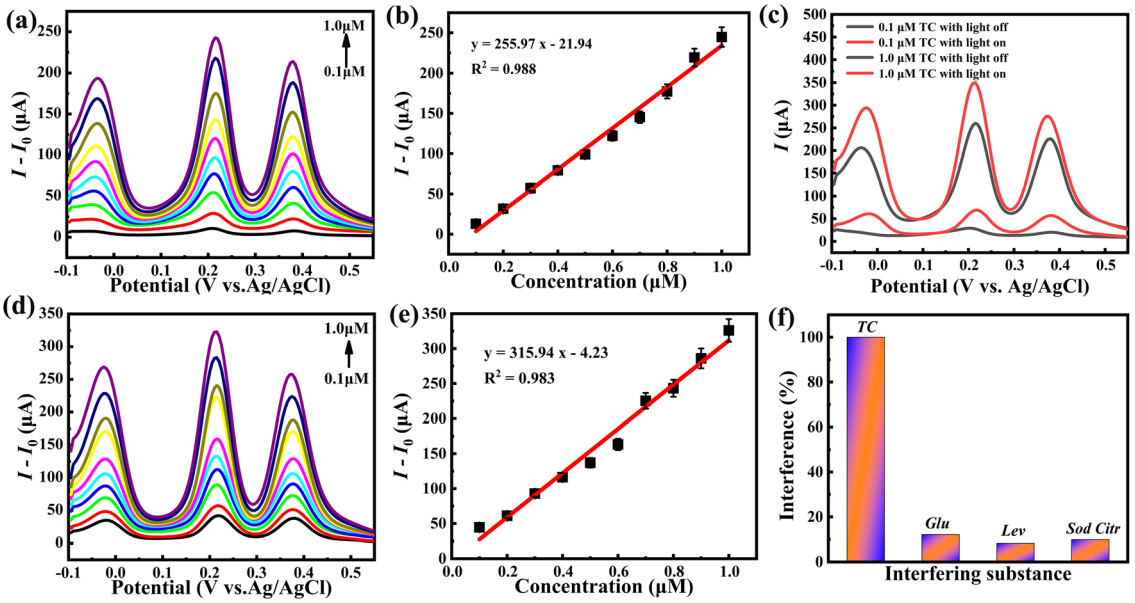

Fig. 6 (a) DPV curves of hybrid **1** modified electrodes in 0.5 M H_2SO_4 with continuous addition of TC under dark conditions; (b) Corresponding linear dependence plot of **1**; (c) DPV curves of **1** in 0.5 M H_2SO_4 with the addition of 0.1 and 1.0 μM TC under visible light illumination; (d) DPV curves of **1** with successive addition of TC under visible light illumination; (e) The linear dependence curve of **1**; (f) Current interference of **1** towards TC with different interferents of 1 mM glucose, levofloxacin and sodium citrate to mix with 1 mM TC.

Similarly, hybrid **1** was used to detect the concentration of TC in natural lake water samples and milk samples to further inspect the reliability. Considering that there is a trace TC content in natural lake water and commercial milk samples, a certain amount of TC was added to the acidified actual samples to measure the response current of sensor **1** for TC oxidation. As shown in Fig. 7, the PEC sensor hybrid **1** exhibited a distinct anodic current response with the addition of TC in actual samples. The corresponding linear regression formulas are I (μA) = 314.16 × C (μM) − 15.28 for lake water samples and I (μA) = 193.13 × C (μM) + 5.62 for milk samples, respectively. The sensitivity and LOD of hybrid **1** are 314.16 μA μM^{-1} and 33.64 nM for TC detection in lake water samples, and the sensitivity and LOD of hybrid **1** are 193.13 μA μM^{-1} and 30.66 nM for TC detection in milk samples. These results show good agreements with the performance in pure water systems, suggesting the high practicality of hybrid **1** for TC detection. Otherwise, the photoelectrochemical detection performance of hybrid **1** for TC detection is also comparable with most reported electrochemical sensors (Table 2).

Additionally, the photoelectrochemical durability and structural stability of hybrid **1** were evaluated. As depicted in Fig. S9,† the reaction current remained constant when hybrid **1** operated in a 0.5 M H_2SO_4 solution containing TC for 10 hours. After a long-term photoelectrochemical test, the structure of hybrid **1** was characterized by IR and XRD (Fig. S10†). It can be found that the characteristic absorption bands of hybrid **1** in the IR spectrum after the test are preserved and the XRD patterns remain unchanged, revealing its good structural stability.

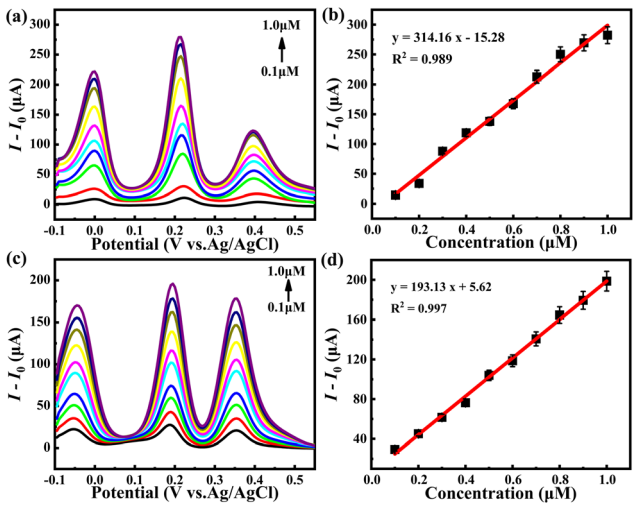

Fig. 7 (a) DPV curves of hybrid **1** in acidified lake water with continuous addition of TC; (b) The linear dependence curve of **1**; (c) DPV curves of hybrid **1** in acidified milk with continuous addition of TC; (d) The linear dependence curve of **1**.

2.6 Photoelectrochemical catalytic mechanism of hybrid 1 for Cr(VI) and TC detection

The above experimental results demonstrated that hybrid **1** is a promising bifunctional PEC sensor for the detection of Cr(VI) and TC.[44–46] To gain more insights, the catalytic mechanisms of the electrocatalytic Cr(VI) reduction[47] and electrooxidation of TC[48] over hybrid **1** were investigated by the chronoamperometry technique. Fig. 8a and b show a sequence of *i*–*t* curves in

Table 2 Comparison of **1** with other reported sensors for the determination of TC

Sensor materials	Method	Dark-LOD (μM)	Light-LOD (μM)	Ref.
1	DPV	0.041	0.033	This work
Fe/Zn-MMT/GCE	DPV	0.10	—	40
GR/L-Cys/GCE	DPV	0.12	—	41
PTH/CNT/CPE	LSV	0.13	—	42
MWNTs-GNPs	CV	0.39	—	43

GCE = glassy carbon electrode; CPE = carbon paste electrode; GNPs = gold nanoparticles.

Cr(VI) and TC solutions with various concentrations. According to the following formula:

$$I_{cat}/I_L = (\pi k_{cat} ct)^{1/2}$$

I_{cat} is the catalytic current after adding Cr(VI) or TC, I_L is the diffusion limited current in the blank solution, t represents the consumed time (s), c stands for the concentration of Cr(VI) or TC solution, k_{cat} is the catalytic rate constant. The relationship between the catalytic current and the reaction time was fitted, and the catalytic rate constant (k_{cat}) can be estimated to be 15.78 mol^{-1} s^{-1} for Cr(VI) reduction and 0.60 mol^{-1} s^{-1} for TC oxidation, respectively. These values indicated the high electrocatalytic activity of hybrid **1** towards Cr(VI) reduction and TC oxidation processes. Moreover, the diffusion coefficients of Cr(VI) and TC over hybrid **1** were also investigated by using the Cottrell equation:

$$I = nFAD^{1/2}c\pi^{-1/2}t^{-1/2}$$

in which D is the diffusion coefficient (cm^2 s^{-1}), n stands for the sum of transferred electrons (n = 3 for Cr(VI) reduction, n = 4 for TC oxidation), A represents the electrode area (0.071 cm^2), I is the peak current dominated by the diffusion of Cr(VI) or TC from the electrolyte to the electrode/electrolyte interface, and c refers to the concentration of added Cr(VI) or TC (mol L^{-1}).

As shown in Fig. 8, the diffusion coefficients are 2.95×10^{-6} cm^2 s^{-1} for Cr(VI) and 2.84×10^{-10} cm^2 s^{-1} for TC, respectively.

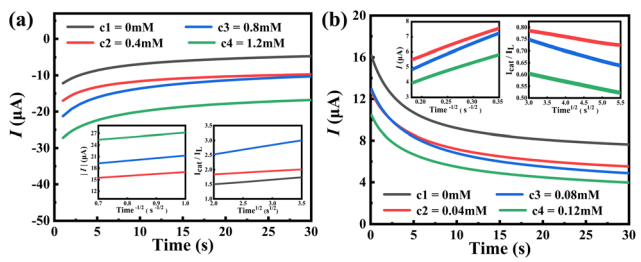

Fig. 8 (a) Chronoamperometry on hybrid **1** after the successive addition of different concentrations of Cr(VI) in 0.5 M H_2SO_4; (b) Chronoamperometry on hybrid **1** after the addition of different concentrations of TC in 0.5 M H_2SO_4. Insets left: plots of I_{cat}/I_L *versus* $t^{1/2}$; right: I *versus* $t^{-1/2}$.

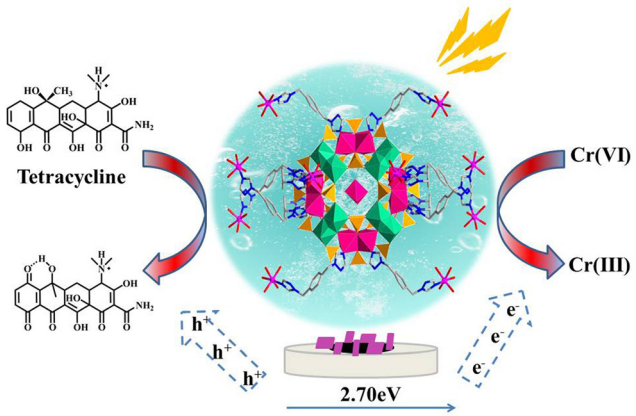

Scheme 1 Photoelectrochemical catalytic mechanisms of hybrid **1** for Cr(VI) and TC detection.

These results demonstrate the favorable diffusion kinetics of Cr(VI) and TC over hybrid **1**, which facilitates the conversion of Cr(VI) reduction and TC oxidation, promoting the photoelectrochemical detection efficiency (Scheme 1).

3. Conclusions

In conclusion, an efficient bifunctional photoelectrochemical sensor based on a wheel-shaped $\{Co_{16}Mo_{16}P_{24}\}$ cluster was synthesized and was used as a photoelectrochemical sensor for the detection of trace Cr(VI) and TC. The $\{Co_{16}Mo_{16}P_{24}\}$ clusters in the hybrid as six-connected nodes extend the structure into a robust 3D framework with a *pcu* topology *via* Co-ligand linkers. With the advantages of wide light-absorption and excellent redox properties, hybrid **1** displayed remarkable photoelectrochemical performance towards the determination of trace Cr(VI) and TC with low detection limits of 24.62 nM for Cr(VI) and 33.45 nM for TC, and the sensitivities of 216.76 μA $μM^{-1}$ for Cr(VI) and 315.94 μA $μM^{-1}$ for TC determination, which far meet the standards set by the WHO and the EU. Moreover, hybrid **1** possesses high anti-interference ability and performs well in the detection of Cr(VI) and TC in lake water and milk samples. This work provides a promising photoelectrochemical sensor for practical environmental pollutant monitoring.

Author contributions

Xiujuan Zhang: methodology, investigation, data curation, writing – original draft, and visualization. Yuanyuan Ma: supervision, writing – review & editing, and resources. Haoxue Bi: investigation. Xiaoyu Yin: data curation. Hao Song: software. Manhui Liu: writing – review & editing. Zhangang Han: writing – review & editing.

Conflicts of interest

There are no conflicts to declare.

Acknowledgements

This research was financially supported by the National Natural Science Foundation of China (Grants 21871076, 21901060), the Natural Science Foundation of Hebei Province (Grants B2020205008, B2022205005, and B2016205051), the Science and Technology Project of Hebei Education Department (Grant BJ2020037), the China Postdoctoral Science Foundation funded Project (No. 2021TQ0095), and the Science Foundation of Hebei Normal University (L2019B15).

References

1 M. B. Arain, I. Ali, E. Yilmaz and M. Soylak, Nanomaterial's based chromium speciation in environmental samples: A review, *TrAC, Trends Anal. Chem.*, 2018, **103**, 44–55.
2 V. I. Mikhaylov, E. F. Krivoshapkina, A. L. Trigub, V. V. Stalugin and P. V. Krivoshapkin, Detection and adsorption of Cr(VI) ions by mesoporous Fe–Alumina films, *ACS Sustainable Chem. Eng.*, 2018, **6**, 9283–9292.
3 D. Fang, T. Xu, L. Fang, H. Chen, Y. Huang, H. Zhang, Z. Miao, C. Mao, B. Chi and H. Xu, A blood compatible, high-efficient sensor for detection of Cr(VI) in whole blood, *Sens. Actuators, B*, 2021, **329**, 129219.
4 G. N. Liu, R. D. Xu, R. Y. Zhao, Y. Sun, Q.-B. Bo, Z. Y. Duan, Y. H. Li, Y. Y. Wang, Q. Wu and C. Li, Hybrid copper iodide cluster-based pellet sensor for highly selective optical detection of o-Nitrophenol and tetracycline hydrochloride in aqueous solution, *ACS Sustainable Chem. Eng.*, 2019, **7**, 18863–18873.
5 S. H. Jalalian, N. Karimabadi, M. Ramezani, K. Abnous and S. M. Taghdisi, Electrochemical and optical aptamer-based sensors for detection of tetracyclines, *Trends Food Sci. Technol.*, 2018, **73**, 45–57.
6 J. Song, X. Lin, N. Jiang and M. Huang, Carbon-doped WO_3 electrochemical aptasensor based on Box-Behnken strategy for highly-sensitive detection of tetracycline, *Food Chem.*, 2022, **367**, 130564.
7 J. Kurittu, S. Lönnberg, M. Virta and M. Karp, A group-specific microbiological test for the detection of tetracycline residues in raw milk, *J. Agric. Food Chem.*, 2000, **48**, 3372–3377.
8 Y. Cao, X. Wang, H. Bai, P. Jia, Y. Zhao, Y. Liu, L. Wang, Y. Zhuang and T. Yue, Fluorescent detection of tetracycline in foods based on carbon dots derived from natural red beet pigment, *LWT – Food Sci. Technol.*, 2022, **157**, 113100.
9 Y. Tian, T. Bu, M. Zhang, X. Sun, P. Jia, Q. Wang, Y. Liu, F. Bai, S. Zhao and L. Wang, Metal-polydopamine framework based lateral flow assay for high sensitive detection of tetracycline in food samples, *Food Chem.*, 2021, **339**, 127854.
10 L. P. Zong, J. Li, G. Shu, X. Liu, R. S. Marks, X. J. Zhang, S. Cosnier and D. Shan, Rational design of a highly dispersed Fe–N–C nanosheet with 1,10-phenanthroline-2,9-dicarboxylic acid as a preorganized ligand: boosted electrochemiluminescence detection of tetracycline, *Anal. Chem.*, 2022, **94**, 1325–1332.
11 Y. Zhang, R. Xu, Q. Kang, Y. Zhang, Q. Wei, Y. Wang and H. Ju, Ultrasensitive photoelectrochemical biosensing platform for detecting N-terminal pro-brain natriuretic peptide based on SnO_2/SnS_2/mpg-C_3N_4 amplified by PbS/SiO_2, *ACS Appl. Mater. Interfaces*, 2018, **10**, 31080–31087.
12 P. J. Babu, A. M. Raichur and M. Doble, Corrigendum to "synthesis and characterization of biocompatible carbon-gold (C-Au) nanocomposites and their biomedical applications as an optical sensor for creatinine detection and cellular imaging", *Sens. Actuators, B*, 2018, **264**, 468.
13 D. Cheng, H. Wu, C. Feng, Y. Ding and H. Mei, Bifunctional photoelectrochemical sensor based on Bi/Bi_2S_3/$BiVO_4$ for detecting hexavalent chromium and hydrogen peroxide, *Sens. Actuators, B*, 2022, **353**, 131108.
14 G. Zhang, D. Cheng, M. Li, C. Feng, H. Wu and H. Mei, Enhanced the photoelectrochemical performance of Bi_2XO_6 (X=W, Mo) for detecting hexavalent chromium by modification of CuS, *J. Environ. Sci.*, 2021, **103**, 185–195.
15 R. S. Moakhar, G. K. L. Goh, A. Dolati and M. Ghorbani, Sunlight-driven photoelectrochemical sensor for direct determination of hexavalent chromium based on Au decorated rutile TiO_2 nanorods, *Appl. Catal., B*, 2017, **201**, 411–418.
16 T. Fang, X. Yang, L. Zhang and J. Gong, Ultrasensitive photoelectrochemical determination of chromium(VI) in water samples by ion-imprinted/formate anion-incorporated graphitic carbon nitride nanostructured hybrid, *J. Hazard. Mater.*, 2016, **312**, 106–113.
17 M. Li, G. Zhang, C. Feng, H. Wu and H. Mei, Highly sensitive detection of chromium(VI) by photoelectrochemical sensor under visible light based on Bi SPR-promoted $BiPO_4$/BiOI heterojunction, *Sens. Actuators, B*, 2020, **305**, 127449.
18 H. Li, J. Li, Y. Qiao, H. Fang, D. Fan and W. Wang, Nano-gold plasmon coupled with dual-function quercetin for enhanced photoelectrochemical aptasensor of tetracycline, *Sens. Actuators, B*, 2017, **243**, 1027–1033.
19 Z. Guo, K. Jiang, H. Jiang, H. Zhang, Q. Liu and T. You, Photoelectrochemical aptasensor for sensitive detection of tetracycline in soil based on CdTe-BiOBr heterojunction: Improved photoactivity enabled by Z-scheme electron transfer pathway, *J. Hazard. Mater.*, 2022, **424**, 127498.
20 J. Gu, W. Chen, G. G. Shan, G. Li, C. Sun, X. L. Wang and Z. Su, The roles of polyoxometalates in photocatalytic reduction of carbon dioxide, *Mater. Today Energy*, 2021, **21**, 100760.
21 F. Li, H. Liu, W. Chen, Y. Su, W. Chen, J. Zhi and Y. Li, Light induced ammonia synthesis by crystalline polyoxometalate-based hybrid frameworks coupled with the Sv-1T MoS_2 cocatalyst, *Inorg. Chem. Front.*, 2022, **9**, 3828–3838.

22 H. Sun, Z. Lang, Y. Zhao, X. Zhao, T. Qiu, Q. Hong, K. Wei, H. Tan, Z. Kang and Y. Li, Copper-bridged tetrakis(4-ethynylphenyl)ethene aggregates with photo-regulated $^1O_2$ and $O_2^{\cdot-}$ generation for selective photocatalytic aerobic oxidation, *Angew. Chem., Int. Ed.*, 2022, **61**, e202202914.

23 J. Du, Y. Y. Ma, H. Tan, Z. H. Kang and Y. Li, Progress of electrochemical CO_2 reduction reactions over polyoxometalate-based materials, *Chin. J. Catal.*, 2021, **42**, 920–937.

24 F. Y. Yu, Z. L. Lang, L. Y. Yin, K. Feng, Y. J. Xia, H. Q. Tan, H. T. Zhu, J. Zhong, Z. H. Kang and Y. G. Li, Pt-O bond as an active site superior to Pt^0 in hydrogen evolution reaction, *Nat. Commun.*, 2020, **11**, 490.

25 F. Y. Yu, Z. L. Lang, Y. J. Zhou, K. Feng, H. Q. Tan, J. Zhong, S. T. Lee, Z. H. Kang and Y. G. Li, Revealing hydrogen evolution performance of single-atom platinum electrocatalyst with polyoxometalate molecular models, *ACS Energy Lett.*, 2021, **6**, 4055–4062.

26 Y. Zhang, J. Liu, S. L. Li, Z. M. Su and Y. Q. Lan, Polyoxometalate-based materials for sustainable and clean energy conversion and storage, *EnergyChem*, 2019, **1**, 100021.

27 C. Du Peloux, A. Dolbecq, P. Mialane, J. Marrot, E. Rivière and F. Sécheresse, A new family of layered molybdenum(v) cobalt-phosphates built up of $[H_{14}(Mo_{16}O_{32})Co_{16}(PO_4)_{24}(H_2O)_{20}]^{10-}$ wheels, *Angew. Chem.*, 2001, **113**, 2521–2523.

28 Y. Ma, Y. Li, E. Wang, Y. Lu, X. Xu and X. Bai, Synthesis, characterization and crystal structure of a new cobalt phosphomolybdate that contains $[(Mo_{16}O_{32})Co_{16}(H_2O)_{18}(PO_4)_6(HPO_4)_{18}]$ wheels, *Transition Met. Chem.*, 2006, **31**, 262–267.

29 H. Miao, H. X. Wan, M. Liu, Y. Zhang, X. Xu, W. W. Ju, D. R. Zhu and Y. Xu, Two novel organic–inorganic hybrid molybdenum(v) cobalt/nickel phosphate compounds based on isolated nanosized Mo/Co(Ni)/P cluster wheels, *J. Mater. Chem. C*, 2014, **2**, 6554–6560.

30 K. Yu, B. B. Zhou, Y. Yu, Z. H. Su and G. Y. Yang, A new organic–inorganic hybrid layered molybdenum(v) cobalt phosphate constructed from $[H_{24}(Mo_{16}O_{32})Co_{16}(PO_4)_{24}(OH)_4(C_5H_4N)_2(H_2O)_6]^{4-}$ wheels and 4,4′-bipyridine linkers, *Inorg. Chem.*, 2011, **50**, 1862–1867.

31 J. Q. Niu, W. T. An, X. J. Zhang, Y. Y. Ma and Z. G. Han, Ultra-trace determination of hexavalent chromium in a wide pH range triggered by heterometallic Cu-Mn centers modified reduced phosphomolybdate hybrids, *Chem. Eng. J.*, 2021, **418**, 129408.

32 W. An, X. Zhang, J. Niu, Y. Ma and Z. Han, Unusual hexanuclear cadmium cluster functionalized phosphomolybdate as effective photoelectrochemical sensor for trace Cr(vi) detection, *Chin. Chem. Lett.*, 2022, **33**, 4400–4404.

33 M. Bravo-Sanchez, A. Romero-Galarza, J. Ramírez, A. Gutiérrez-Alejandre and D. A. Solís-Casados, Quantification of the sulfidation extent of Mo in CoMo HDS catalyst through XPS, *Appl. Surf. Sci.*, 2019, **493**, 587–592.

34 X. Xin, N. Hu, Y. Ma, Y. Wang, L. Hou, H. Zhang and Z. Han, Polyoxometalate-based crystalline materials as a highly sensitive electrochemical sensor for detecting trace Cr(vi), *Dalton Trans.*, 2020, **49**, 4570–4577.

35 S. Adhikari, S. Mandal and D. H. Kim, 1D/2D constructed $Bi_2S_3/Bi_2O_2CO_3$ direct Z-Scheme heterojunction: A versatile photocatalytic material for boosted photodegradation, photoreduction and photoelectrochemical detection of water-based contaminants, *J. Hazard. Mater.*, 2021, **418**, 126263.

36 Y. Zhang, P. Chen, F. Wen, B. Yuan and H. Wang, Fe_3O_4 nanospheres on MoS_2 nanoflake: electrocatalysis and detection of Cr(vi) and nitrite, *J. Electroanal. Chem.*, 2016, **761**, 14–20.

37 J. Tu, Y. Gan, T. Liang, H. Wan and P. Wang, A miniaturized electrochemical system for high sensitive determination of chromium(vi) by screen-printed carbon electrode with gold nanoparticles modification, *Sens. Actuators, B*, 2018, **272**, 582–588.

38 O. Domínguez-Renedo, L. Ruiz-Espelt, N. García-Astorgano and M. J. Arcos-Martínez, Electrochemical determination of chromium(VI) using metallic nanoparticle-modified carbon screen-printed electrodes, *Talanta*, 2008, **76**, 854–858.

39 L. Jin, J. Ying, Y. Zhang, C. Sun, A. Tian and X. Wang, A series of polyoxometalate compounds by tuning N sites and numbers of ligands: syntheses, characterization and electrochemical sensing, and photocatalytic and supercapacitor properties, *New J. Chem.*, 2022, **46**, 8422–8432.

40 T. Gan, Z. Shi, J. Sun and Y. Liu, Simple and novel electrochemical sensor for the determination of tetracycline based on iron/zinc cations–exchanged montmorillonite catalyst, *Talanta*, 2014, **121**, 187–193.

41 X. M. Sun, Z. Ji, M. X. Xiong and W. Chen, The electrochemical sensor for the determination of tetracycline based on graphene/l-cysteine composite film, *J. Electrochem. Soc.*, 2017, **164**, B107–B112.

42 Z. Jahromi, M. Afzali, A. Mostafavi, R. Nekooie and M. Mohamadi, Electropolymerization of thionine as a stable film along with carbon nanotube for sensitive detection of tetracycline antibiotic drug, *Iran. Polym. J.*, 2020, **29**, 241–251.

43 H. Wang, H. Zhao, X. Quan and S. Chen, Electrochemical determination of tetracycline using molecularly imprinted polymer modified carbon nanotube-gold nanoparticles electrode, *Electroanalysis*, 2011, **23**, 1863–1869.

44 S. Srinivas and A. S. Kumar, High-performance electrocatalytic reduction and sensing of hazardous hexavalent chromium using a redox-active binol species-impregnated carbon nanofiber-modified electrode, *J. Phys. Chem. C*, 2022, **126**, 8296–8311.

45 H. Guo, Y. Su, Y. Shen, Y. Long and W. Li, In situ decoration of Au nanoparticles on carbon nitride using a single-source precursor and its application for the detection of tetracycline, *J. Colloid Interface Sci.*, 2019, **536**, 646–654.

46 X. Zhao, X. Wang, Y. Zhao, H. Sun, H. Tan, T. Qiu, Z. Zhao, X. Zhao, S. Cheng and Y. Li, Polyoxometalates-doped TiO_2/Ag hybrid heterojunction: removal of multiple pollutants and mechanism investigation, *Environ. Sci. Nano*, 2021, **8**, 3855–3864.
47 Q. Ji, D. Yu, G. Zhang, H. Lan, H. Liu and J. Qu, Microfluidic flow through polyaniline supported by lamellar-structured graphene for mass-transfer-enhanced electrocatalytic reduction of hexavalent chromium, *Environ. Sci. Technol.*, 2015, **49**, 13534–13541.
48 X. Dang, C. Hu, Y. Wei, W. Chen and S. Hu, Sensitivity improvement of the oxidation of tetracycline at acetylene black electrode in the presence of sodium dodecyl sulfate, *Electroanalysis*, 2004, **16**, 1949–1955.